Supporting Information for

Vacancy-engineered g-C_3N_4 with modulated p-band center for highly selective photocatalytic H_2O_2 production in pure water

Zonglin Jiang [1], Fangyu Zhai [1], Zedong Lu [2], Chen Li (✉)[1], Mingxin Li [1], Ke Wang [1], Fei Qi [1], Fan Li [1], Zhenbei Wang [1], Yatao Liu [1], Oksana Ismailova [3, 4], Zuhra Kadirova [3], Amir Ikhlaq [5], Jing Kang (✉)[6]

1 Beijing Key Lab for Source Control Technology of Water Pollution, College of Environmental Science and Engineering, Beijing Forestry University, Beijing 100083, China

2 College of Architecture & Civil Engineering, Beijing University of Technology, Beijing 100124, China

3 Uzbekistan-Japan Innovation Center of Youth, Tashkent State Technical University, Tashkent 100095, Uzbekistan

4 Turin Polytechnic University Tashkent, Tashkent 100095, Uzbekistan

5 Institute of Environment Engineering and Research, University of Engineering and Technology, Lahore 54890, Pakistan

6 State Key Laboratory of Urban-rural Water Resources and Environment, School of Environment, Harbin Institute of Technology, Harbin 150090, China

✉ Corresponding authors

E-mail: li_c21@bjfu.edu.cn (C. Li); jingkanghit@163.com (J. Kang)

Text S1. H_2O_2 detection methods

Amplex Red is a highly sensitive fluorogenic probe for detecting H_2O_2 in the presence of horseradish peroxidase (HRP). Through HRP-catalyzed oxidation, Amplex Red reacts stoichiometrically with H_2O_2 to generate resorufin, a red-fluorescent product. The reaction proceeds as follows (Eq. (S1)):

$$\text{Amplex red} + H_2O_2 \xrightarrow{\text{HRP}} \text{Resorufin} \quad \text{(S1)}$$

The fluorescence intensity of resorufin can be quantitatively measured using a fluorescence microplate reader at excitation/emission wavelengths of 571 nm/587 nm.

To establish a standard calibration curve, a series of H_2O_2 solutions with concentrations were analyzed using the Amplex Red/HRP detection system. Fluorescence emission at 587 nm was recorded and plotted against H_2O_2 concentrations.

Text S2. Dynamic Kinetic Analysis of H_2O_2 Formation and Decomposition

According to Equation 1-4, zero-order kinetics (H_2O_2 formation) and first-order kinetics (H_2O_2 decomposition) models were respectively established to evaluate the reaction kinetics of photocatalytic H_2O_2 production(Shiraishi et al., 2014; Chu et al., 2020).

$$H_2O_2 + H^+ + e^- \rightarrow H_2O + \cdot OH \quad \text{(S2)}$$

$$H_2O_2 + 2H^+ + 2e^- \rightarrow 2H_2O \quad \text{(S3)}$$

$$H_2O_2 + h^+ \rightarrow \cdot HO_2 + H^+ \quad \text{(S4)}$$

$$H_2O_2 + 2h^+ \rightarrow O_2 + 2H^+ \quad \text{(S5)}$$

$$C_{(H_2O_2)} = \frac{k_f}{k_d}[1\text{-}\exp(-k_d t)] \quad \text{(S6)}$$

k_f—the formation constant of H_2O_2 (μmol/L/min);

k_d—the decomposition constant of H_2O_2 (1/min);

t—the reaction time (s)

Text S3. Photoelectrochemical measurements

Electrochemical measurements were performed on an electrochemical workstation (CHI660C, China) using a standard three-electrode system. Pt sheet electrode and Ag/AgCl electrode were separately used as the counter electrode and reference electrode. Typically, 20 mg of powder sample was dispersed in a mixed solution (300 μL ethanol and 20 μL Nafion) and sonicated for 30 min. Then the resulting suspension was dip-coated on the electrode surface and dried overnight at room temperature. All electrochemical tests were carried out by using 0.5 mol/L Na_2SO_4 solution as the electrolyte.

The rotating ring-disk electrode (RRDE) measurements were performed on a CHI Instruments CHI660C advanced electrochemical system with a three-electrode cell using a saturated calomel electrode and a C rod electrode as the reference and counter electrode, respectively. The working electrode was prepared as follows: catalysts (3 mg) were dispersed in IPA (0.5 mL) containing 20μL Nafion (5 wt%) by ultrasonication. The slurry (5 μL) was put onto a disk electrode and dried at room temperature. The linear sweep voltammogram (LSV) were obtained in an O_2-saturated 0.1 mol/L phosphate buffer solution (pH 7.6) with a scan rate 10 mV/s. The electron transfer number involved in the overall O_2 reduction was determined by the slopes of the Koutecky–Levich plots with the following equations:

$$j^{-1} = j_k^{-1} + B^{-1}\omega^{-1/2} \quad \text{(S7)}$$

$$k\ (\text{slope}) = B^{-1} \quad \text{(S8)}$$

$$B = 0.2nFv^{-1/6}CD^{2/3} \quad \text{(S9)}$$

Where j is the current density, j_k is the kinetic current density, ω is the rotating speed (rpm), F is the Faraday constant (96485 C/mol), ν is the kinetic viscosity of water (0.01 cm^2/s), C is the bulk concentration of O_2 in water (1.2×10^{-6} mol/cm^3), and D is the diffusion coefficient of O_2 (1.9×10^{-5} cm^2/s), respectively.

Using the Mott-Schottky equation S10, we can determine the carrier density N_d and the flat band potential V_{fb} (Gelderman et al., 2007; Li et al., 2017).

$$\frac{1}{C^2} = \frac{2}{\varepsilon\varepsilon_0 A^2 e N_d}\left(V - V_{fb} - \frac{kT}{e}\right) \quad \text{(S10)}$$

Where:

C - capacitance

ε- the relative permittivity of the semiconductor material

ε_0 – the vacuum permittivity (8.854×10^{-12} F/m)

e- the electron charge (1.602×10^{-19} C)

N_d – the carrier density

V – the electrode potential (V)

V_{fb} – the flat band potential(V)

k – the boltzmann constant (1.38×10^{-23}J/K)

T – the temperature (K), typically around 298 K at room temperature

At 1000 Hz, the relative permittivity of carbon nitride is 7.5 (Patra and Mohapatra, 2021). The last term kT/e is often neglected in calculations (Gelderman et al., 2007; Li et al., 2017).

Text S4. DFT calculation

The corresponding band structures and density of state (DOS) are calculated using the Vienna Ab-initio simulation package (VASP) codes with the projector augmented wave (PAW) potentials. We employ the Perdew-Burke- Ernzerhof of generalized gradient approximation (GGA-PBE) for exchange- correlation energy. Given the weak interactions between g-C_3N_4 and the adsorbates, van der Waals interactions were accounted for using the PBE-D_2 method. The cutoff energy for the plane-wave basis, the self-consistent total-energy difference and the convergence criterion for forces on atoms were set to 450 eV, 10^{-4} eV and 0.02 eV/Å, respectively. A 1 × 1 × 2 Monkhorst–Pack k-point grid was used to sample the first Brillouin zone

for the band-structure and DOS calculations.

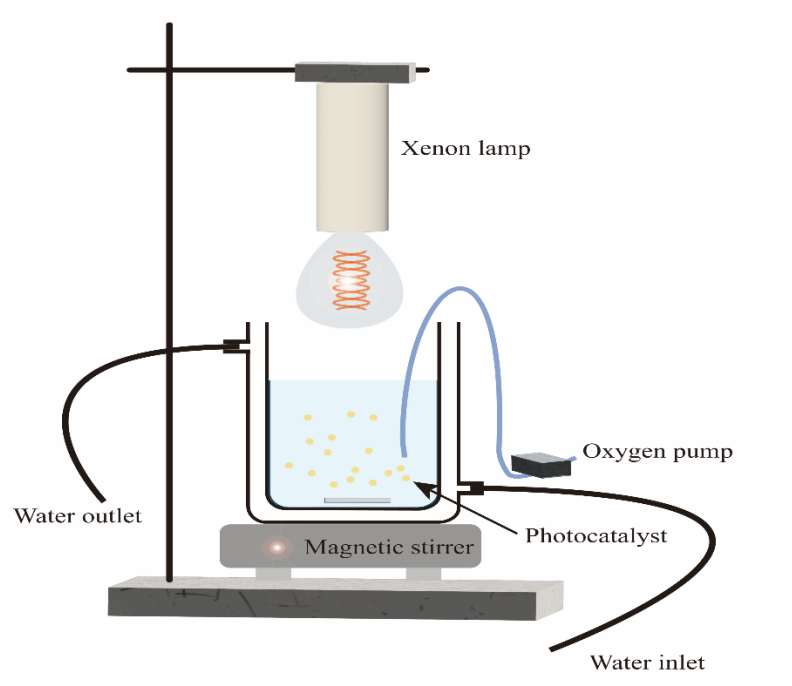


Figure S1. The Schematic diagram of the photocatalytic hydrogen peroxide production experimental setup.

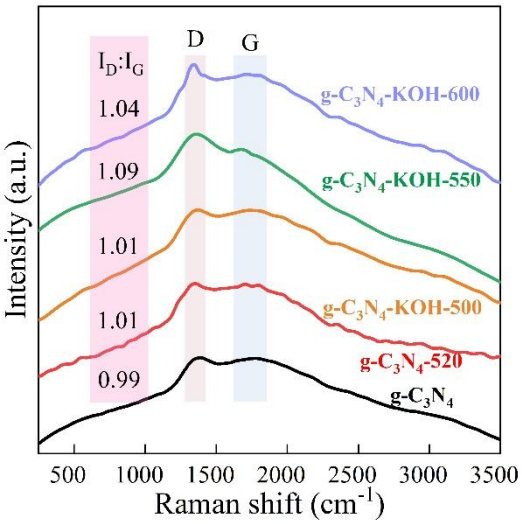


Figure S2. Raman spectra of g-C_3N_4, g-C_3N_4-520, g-C_3N_4-KOH-500, g-C_3N_4-KOH-550, and g-C_3N_4-KOH-600.

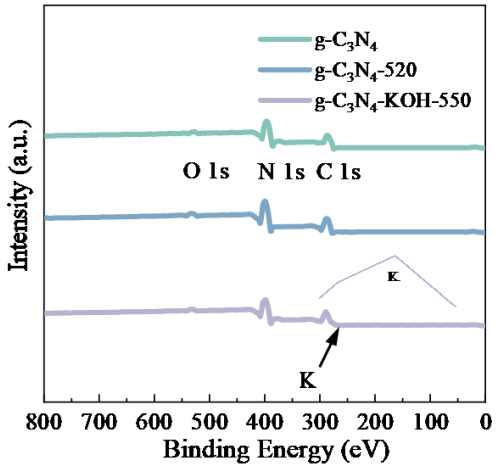


Figure S3. Survey XPS spectra of g-C_3N_4-520, g-C_3N_4-KOH-550, and g-C_3N_4.

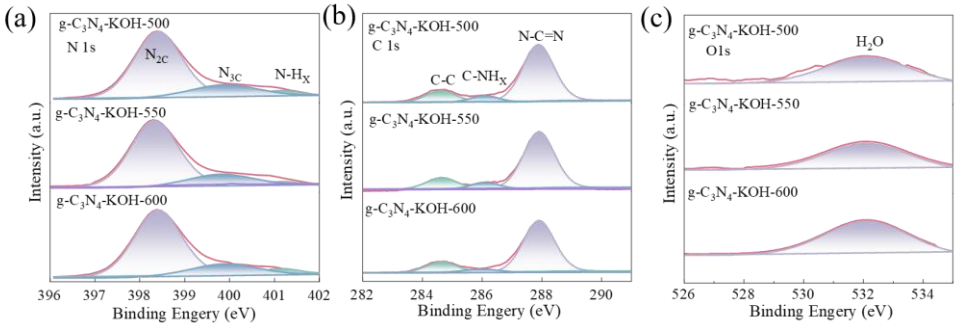


Figure S4. XPS spectra of (a) N 1s, (b) C 1s, and (c) O 1s for the g-C_3N_4-KOH-500, g-C_3N_4-KOH-550, and g-C_3N_4-KOH-600.

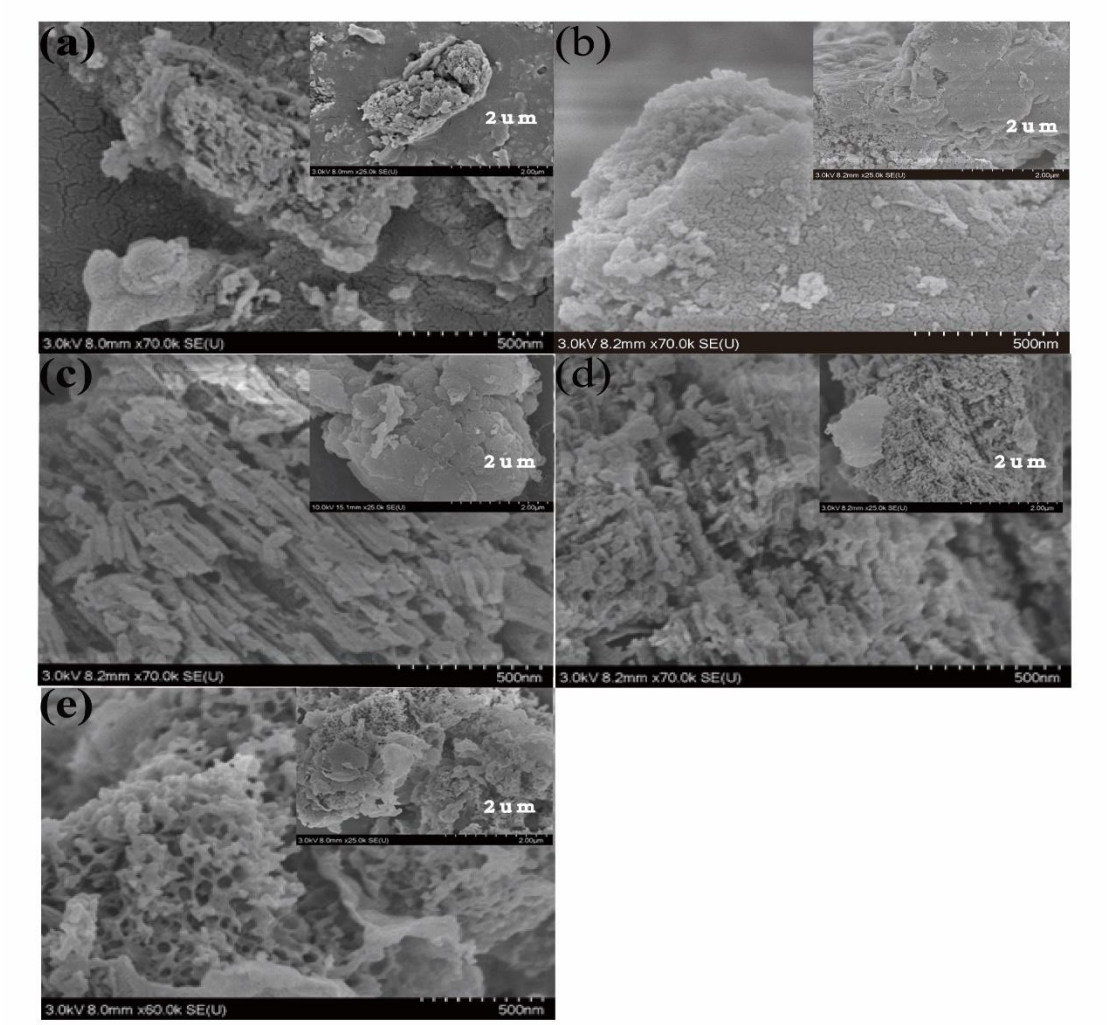
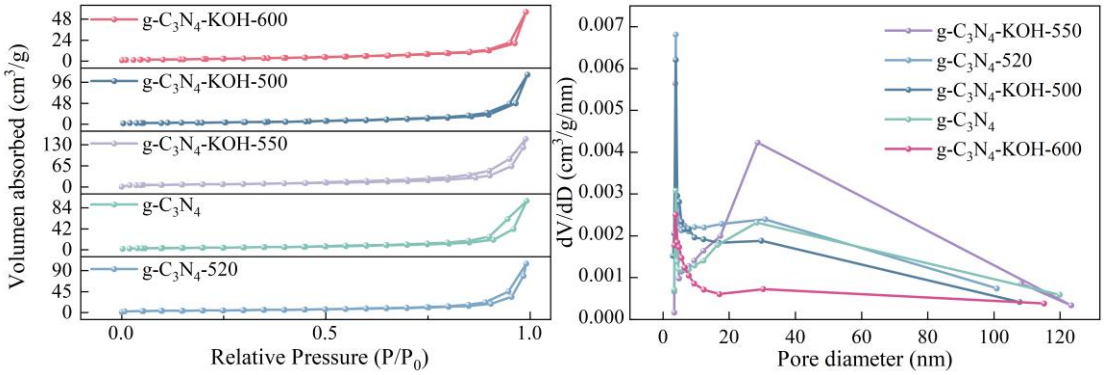


Figure S5. SEM images of (a) g-C_3N_4, (b) g-C_3N_4-520, (c) g-C_3N_4-KOH-500, (d) g-C_3N_4-KOH-550, and (e) g-C_3N_4-KOH-600.



(a) (b)

Figure S6. (a) N_2 sorption isotherms and (b) pore size distribution curves for g-C_3N_4, g-C_3N_4-520, g-C_3N_4-KOH-500, g-C_3N_4-KOH-550, and g-C_3N_4-KOH-600.

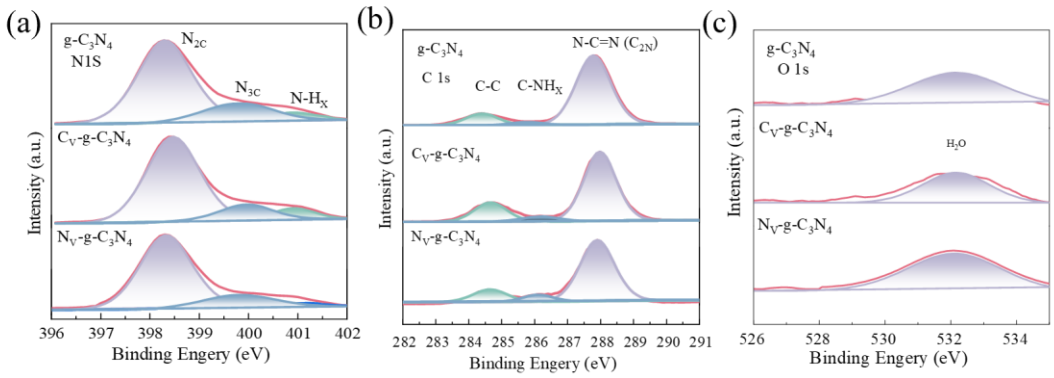


Figure S7. XPS spectra of (a) N 1s, (b) C 1s, and (c) O 1s for the g-C_3N_4, C_V-g-C_3N_4, and N_V-g-C_3N_4.

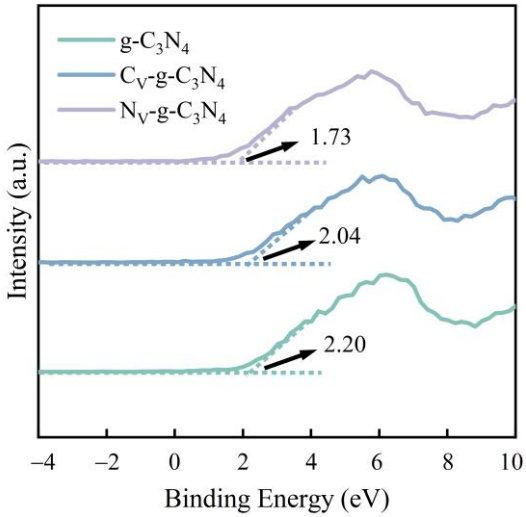


Figure S8. Valence band spectra of g-C_3N_4, C_V-g-C_3N_4, and N_V-g-C_3N_4 of XPS VB.

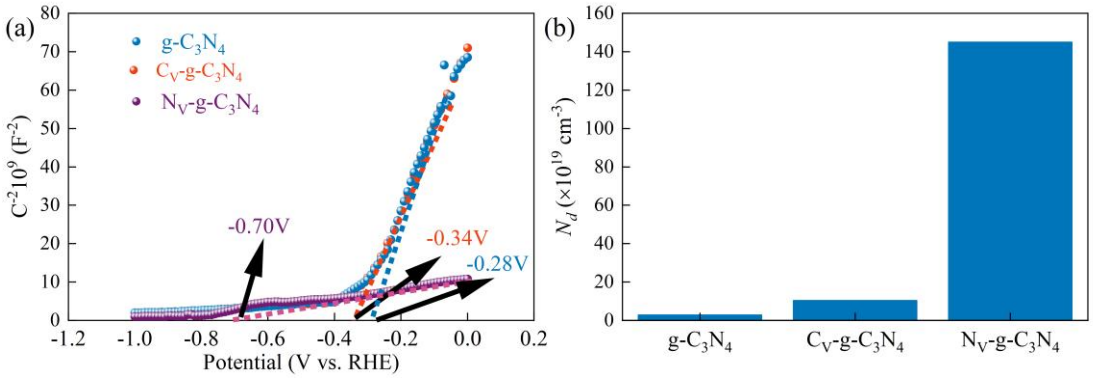


Figure S9. Mott–Schottky plots (a) and carrier densities (N_d) (b) of g-C_3N_4, C_V-g-C_3N_4, and N_V-g-C_3N_4. The N_d of g-C_3N_4, C_V-g-C_3N_4, and N_V-g-C_3N_4 are derived from the slopes of the Mott–Schottky plots.

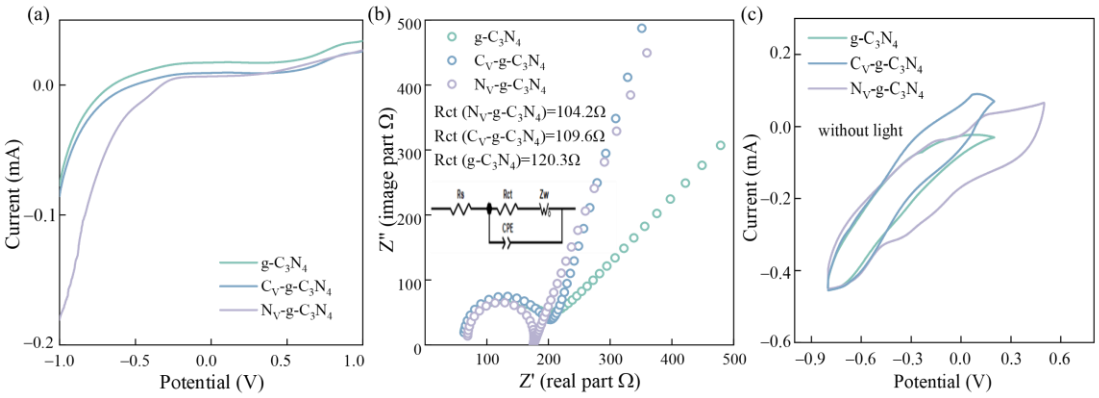


Figure S10. (a) LSV, (b) EIS, and (c) CV under dark of g-C_3N_4, C_V-g-C_3N_4, and N_V-g-C_3N_4.

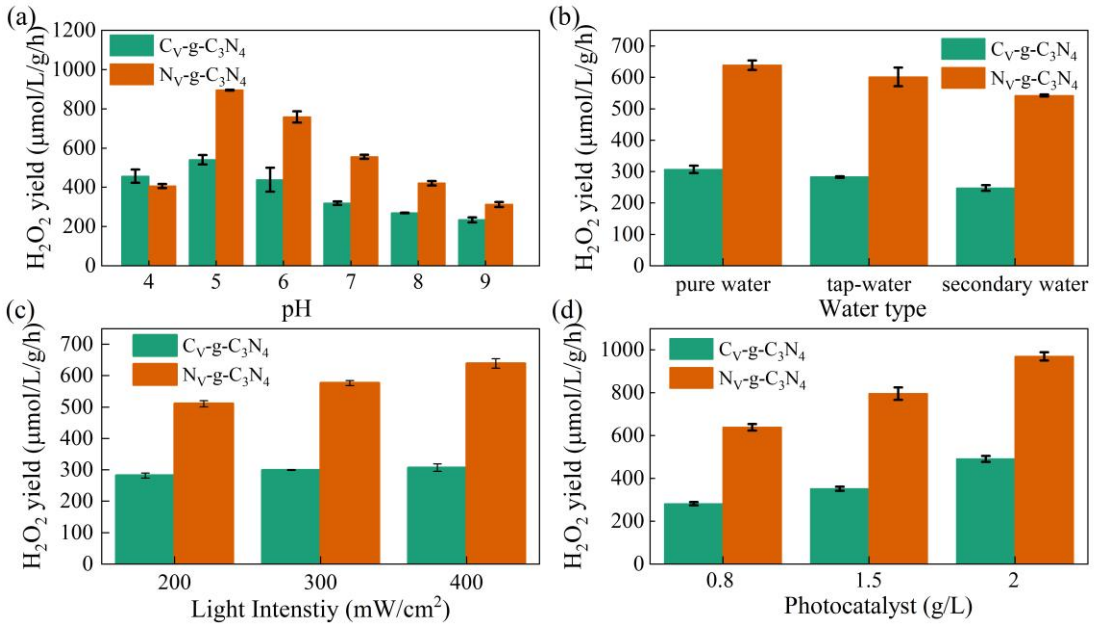


Figure S11. Impacts of various factors on photocatalytic H_2O_2 production experiments for N_V-g-C_3N_4 and C_V-g-C_3N_4 with respect to (a) pH, (b)water body, (c) light intensity, and (d) catalyst concentration.

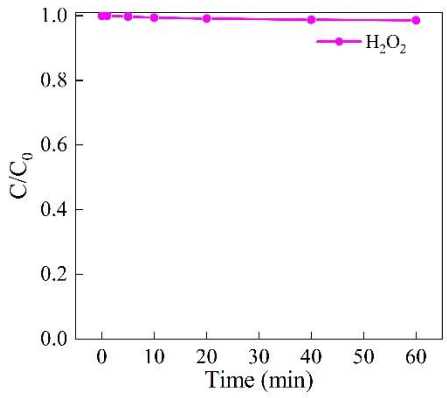


Figure S12. Self-decomposition of H_2O_2 under the reaction conditions in the absence of catalyst.

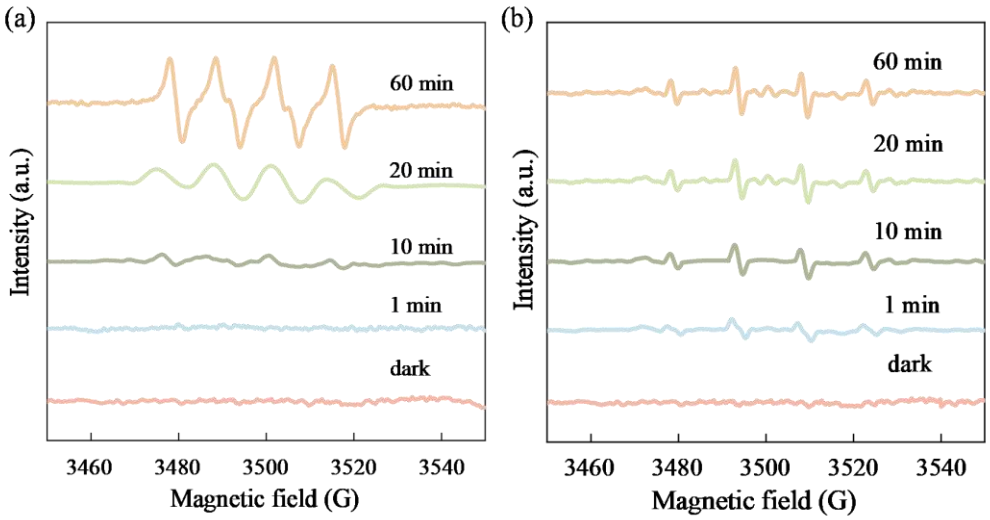


Figure S13. EPR spectra of (a) DMPO-·O_2^- and (b) DMPO-·OH for C_V-g-C_3N_4 in dark and under light conditions.

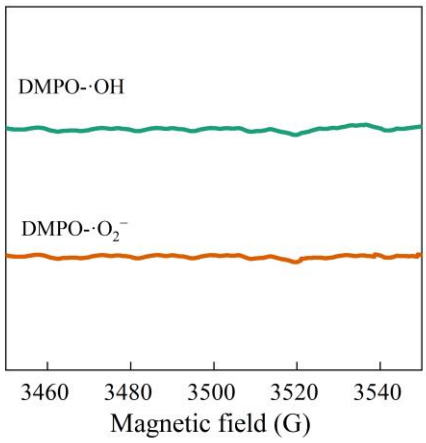


Figure S14. EPR spectra of DMPO-·O_2^- and DMPO-·OH for g-C_3N_4 in light conditions.

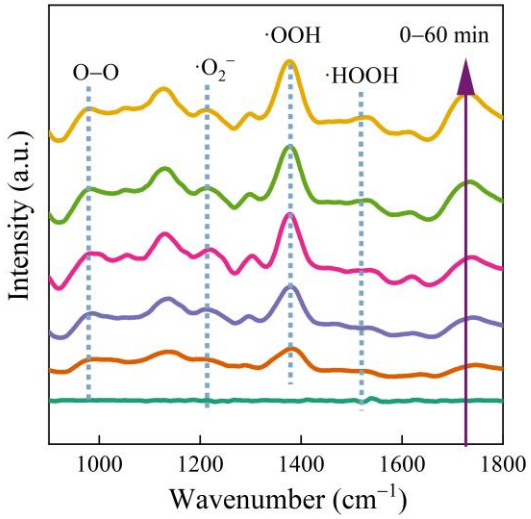


Figure S15. In situ DRIFTS spectra of C_V-g-C_3N_4.

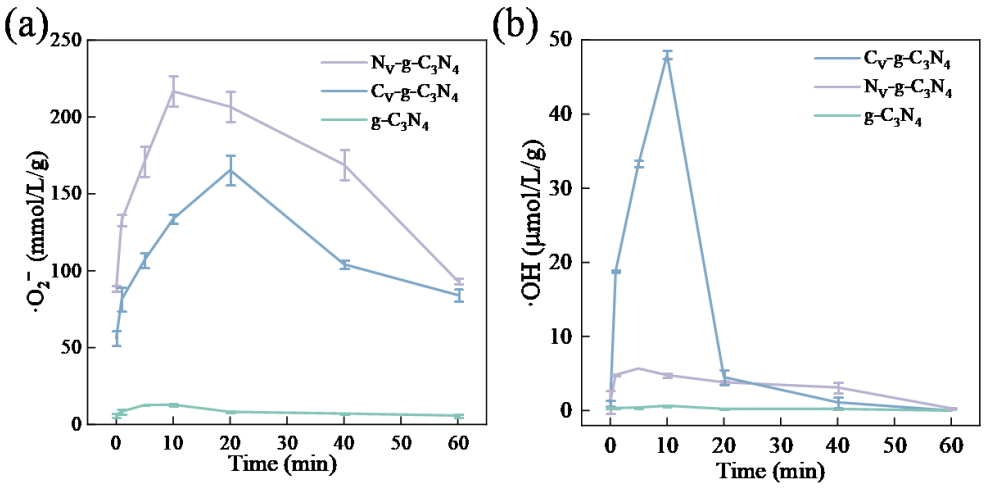


Figure S16. The yields of $\cdot O_2^-$ (a) and ·OH (b) for g-C_3N_4, C_V-g-C_3N_4, and N_V-g-C_3N_4.

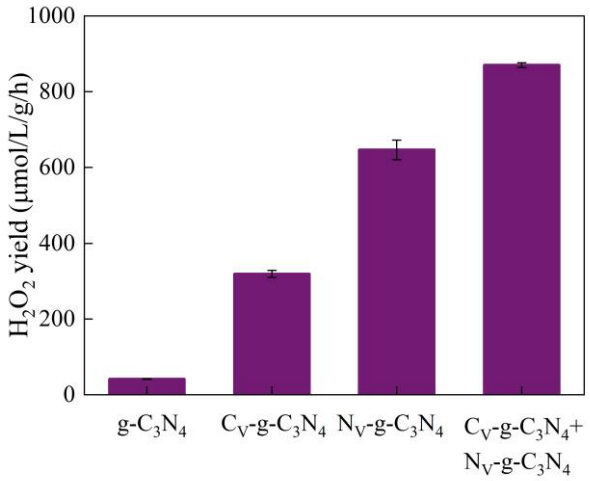


Figure S17. Photocatalytic experiments for H_2O_2 production of g-C_3N_4, C_V-g-C_3N_4, N_V-g-C_3N_4, and the physical mixture of C_V-g-C_3N_4 and N_V-g-C_3N_4

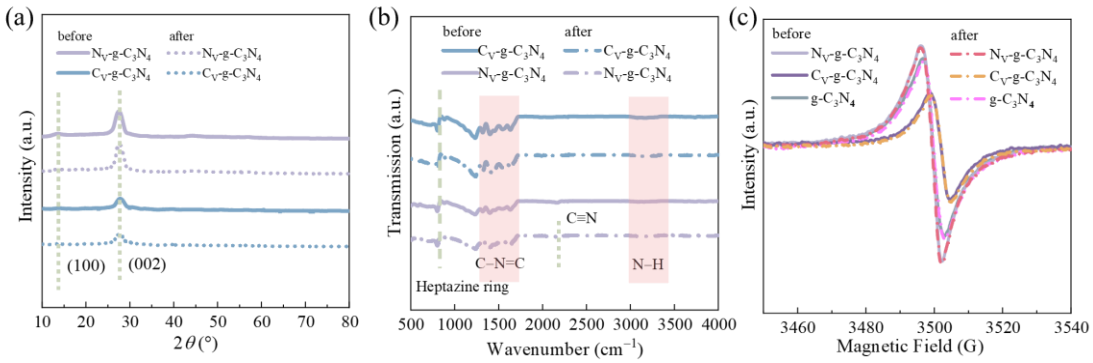


Figure S18. (a) XRD, (b) FTIR, and (c) EPR of g-C_3N_4, C_V-g-C_3N_4, and N_V-g-C_3N_4 before and after the reaction.

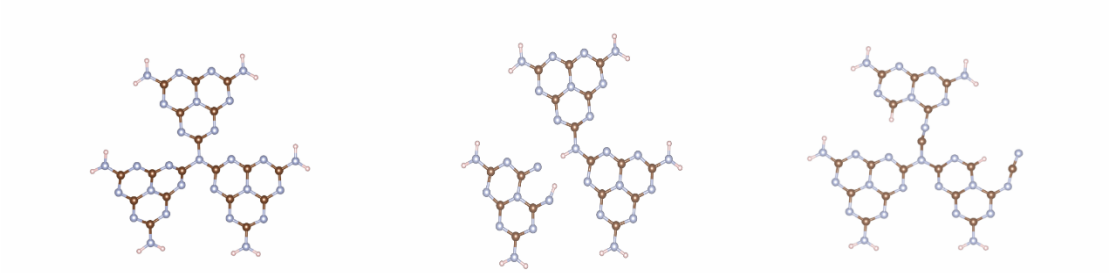


Figure S19. g-C_3N_4, C_V-g-C_3N_4, and N_V-g-C_3N_4 with different structural unit.

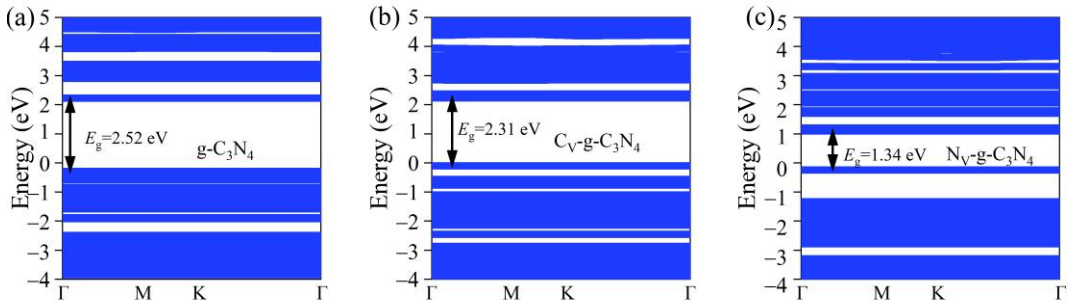


Figure S20. Calculated Eg of (a) g-C_3N_4, (b) C_V-g-C_3N_4, (c) and N_V-g-C_3N_4.

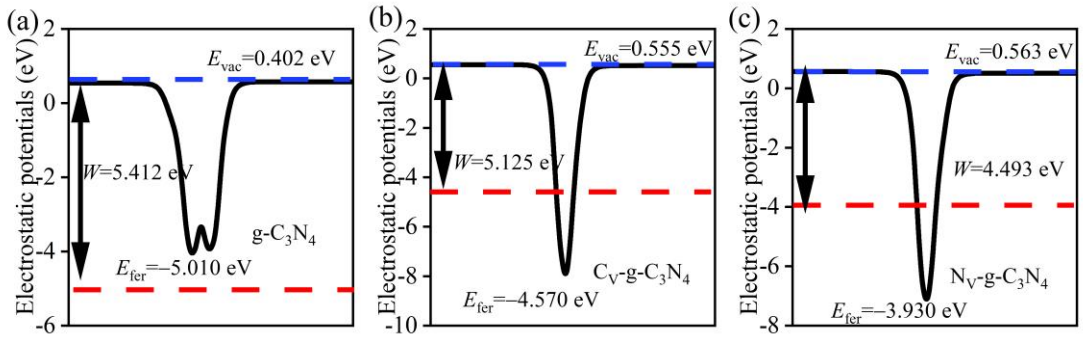


Figure S21. The work functions of (a) g-C_3N_4, (b) C_V-g-C_3N_4, and (c) N_V-g-C_3N_4.

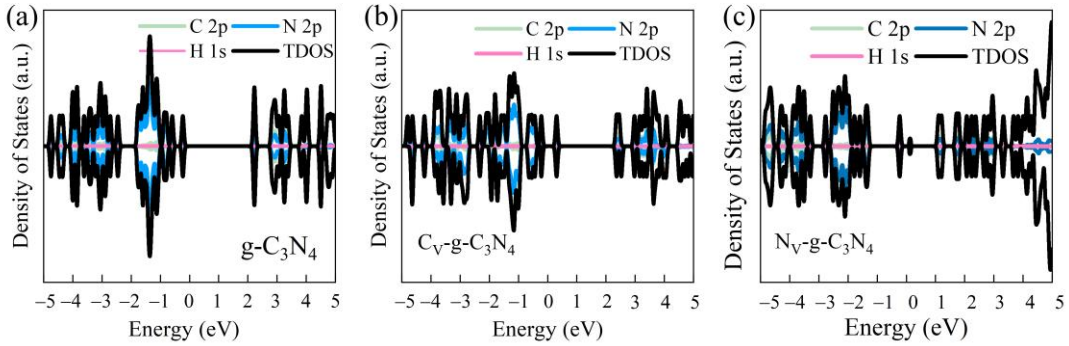


Figure S22. Calculated DOS of (a) g-C_3N_4, (b) C_V-g-C_3N_4, and (c) N_V-g-C_3N_4.

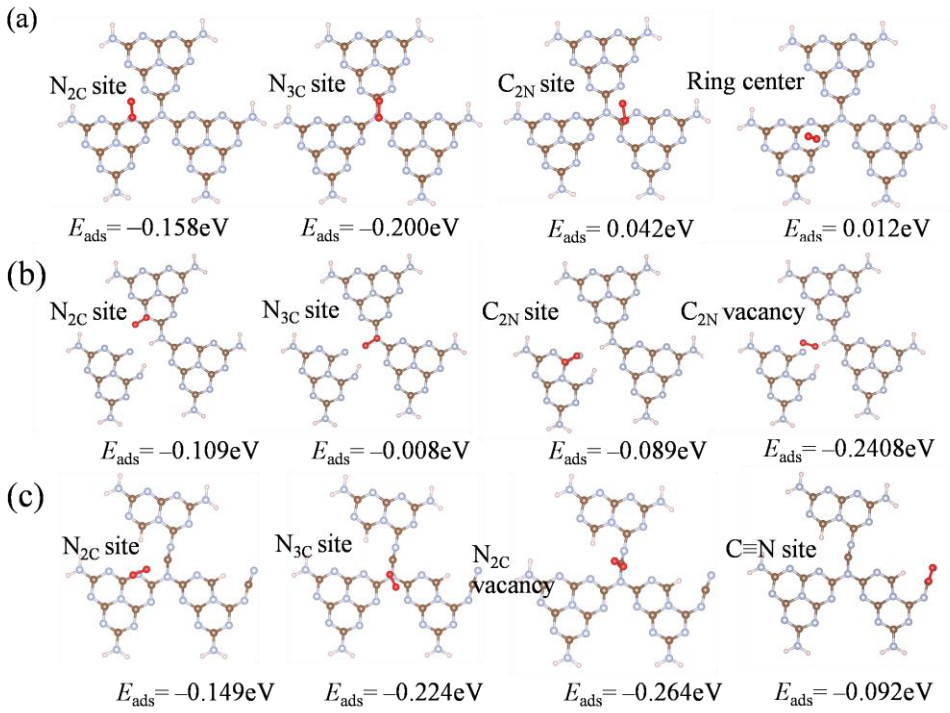


Figure S23. The Gibbs free energies for adsorption of O_2 molecules of g-C_3N_4 (a), C_V-g-C_3N_4 (b), and N_V-g-C_3N_4 (c) at different sites.

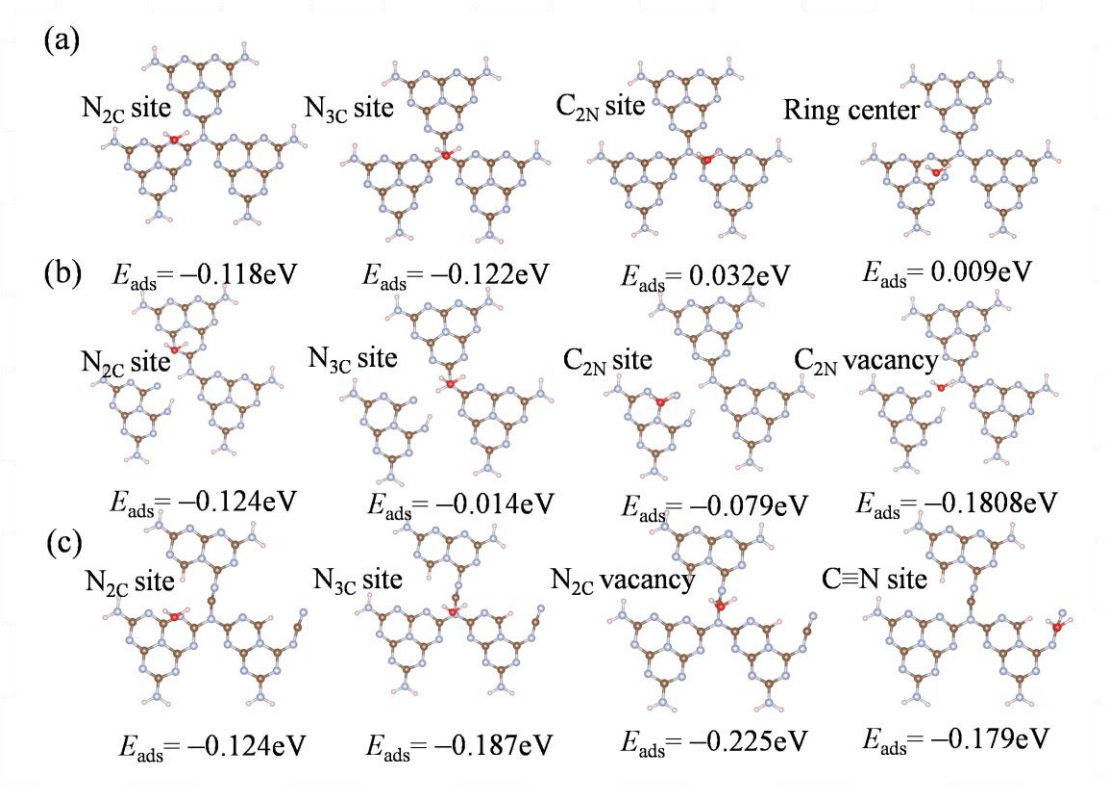


Figure S24. The Gibbs free energies for adsorption of H_2O molecules of g-C_3N_4 (a), C_V-g-C_3N_4 (b), and N_V-g-C_3N_4 (c) at different sites.

Table S1. Textural properties of different g-C_3N_4-based photocatalysts

Sample	Area (m^2/g)	pore volume (cm^3/g)	Pore size (nm)
g-C_3N_4	7.507	0.1516	3.796
C_V-g-C_3N_4	8.475	0.1626	3.817
g-C_3N_4-KOH-500	8.786	0.1750	3.842
g-C_3N_4-KOH-550	9.937	0.2282	3.801
g-C_3N_4-KOH-600	9.054	0.0872	3.793

Table S2. Summary of the photocatalytic production of H_2O_2 with other g-C_3N_4-based photocatalysts

Serial number	Photocatalyst	Reaction solution	Light source	Surface-area-normalized H_2O_2 production rate ($\mu mol/L/m^2/h$)	Reference
1	NCH	10% EtOH	320nm < λ < 780nm	3.27	(Zhu et al., 2022)
2	g-C_3N_4-CoWO	distilled water	λ>420 nm	4.01	(Zhao and Zhao, 2019)
3	CN-ND	5% EtOH	420nm < λ < 800nm	5.57	(Fattahimoghaddam et al., 2021)
4	g-C_3N_4-nv	distilled water	λ>420 nm	14.02	(Lu et al., 2024)
5	g-C_3N_4-PWO	distilled water	λ>420 nm	36.84	(Zhao and Zhao, 2018)
6	g-C_3N_4 with defect	20% isopropanol	λ>420 nm	38.59	(Shi et al., 2018)
7	B/g-C_3N_4	10% isopropanol	420nm < λ < 800nm	40.93	(Ding et al., 2022b)

8	Ti_3C_2/ g-C_3N_4	10% isopropanol	λ> 420 nm	44.49	(Yang et al., 2019b)
9	g-C_3N_4-WSe_2	distilled water	λ>420 nm	49.36	(Tan et al., 2022)
10	CCN-SA/t-KF	10% TEOA	AM 1.5G	54.52	(Hasnan et al., 2023)
11	3D-CN-C1	5% isopropanol	λ>420 nm	57.1	(Ding et al., 2022a)
12	DPCN-520	10% EtOH	λ>420 nm	65.1	(Tian et al., 2023)
13	Nv-g-C_3N_4	deionized water	λ>420 nm	65.3	this work

Table S3. XPS spectra of C 1s and N 1s for g-C_3N_4, C_V-g-C_3N_4, and N_V-g-C_3N_4 before and after the reaction

Photocatalyst	Condition	C 1s Peaks (eV)			N 1s Peaks (eV)		
		C-C (%)	C-NH_X (%)	N-C=N (%)	N_{2C} (%)	N_{3C} (%)	N-H_X (%)
g-C_3N_4	before	12.9	4.8	82.3	80.9	18.3	0.8
	after	14.4	4.1	81.5	80.4	19.1	0.5
C_V-g-C_3N_4	before	20.4	5.7	73.9	80.7	18.1	1.2
	after	22.3	6.4	71.3	81.4	17.9	0.7
N_V-g-C_3N_4	before	15.2	8.3	76.5	73.6	26.2	0.2
	after	16.2	8.6	75.2	71.5	28.4	0.1

Uncategorized References

Acharya L, Mishra B P, Pattnaik S P, Acharya R, Parida K (2022). Incorporating nitrogen vacancies in exfoliated B-doped g-C_3N_4 towards improved photocatalytic ciprofloxacin degradation and hydrogen evolution. New Journal of Chemistry, 46(7): 3493-3503

An J, Wang Z, Liu G, Li L, Tang B (2025). Enhanced photocatalytic H_2O_2 yield by single-atom Pt decorated carbon nitride sheets via boosting *OOH intermediate generation. Journal of Materials Chemistry A, 13(27): 21797-21807

Chen L, Chen C, Yang Z, Li S, Chu C, Chen B (2021). Simultaneously Tuning Band Structure and Oxygen Reduction Pathway toward High-Efficient Photocatalytic Hydrogen Peroxide Production Using Cyano-Rich Graphitic Carbon Nitride. Advanced Functional Materials, 31(46): 2105731

Chen X, Gu H, Qin L, Kang S-Z, Li X (2020). Facile fabrication of adjustable Al/C_3N_4/Agx nano-micro composites for sensitive SERS detection. Materials & Design, 191: 108609

Chu C, Zhu Q, Pan Z, Gupta S, Huang D, Du Y, Weon S, Wu Y, Muhich C, Stavitski E, Domen K, Kim J-H (2020). Spatially separating redox centers on 2D carbon nitride with cobalt single atom for photocatalytic H_2O_2 production. Proceedings of the National Academy of Sciences, 117(12): 6376-6382

Ding Y, Maitra S, Esteban D A, Bals S, Vrielinck H, Barakat T, Roy S, Van Tendeloo G, Liu J, Li Y, Vlad A, Su B-L (2022a). Photochemical production of hydrogen peroxide by digging pro-superoxide radical carbon vacancies in porous carbon nitride. Cell Reports Physical Science, 3(5): 100874

Ding Y, Maitra S, Wang C, Zheng R, Zhang M, Barakat T, Roy S, Liu J, Li Y, Hasan T, Su B-L (2022b). Hydrophilic bi-functional B-doped g-C_3N_4 hierarchical architecture for excellent photocatalytic H_2O_2 production and photoelectrochemical water splitting. Journal of Energy Chemistry, 70: 236-247

Ding Z, Chen X, Antonietti M, Wang X (2011). Synthesis of Transition Metal-Modified Carbon Nitride Polymers for Selective Hydrocarbon Oxidation. ChemSusChem, 4(2): 274-281

Fattahimoghaddam H, Mahvelati-Shamsabadi T, Lee B-K (2021). Enhancement in Photocatalytic H_2O_2 Production over g-C_3N_4 Nanostructures: A Collaborative Approach of Nitrogen Deficiency and Supramolecular Precursors. ACS Sustainable Chemistry & Engineering, 9(12): 4520-4530

Gelderman K, Lee L, Donne S W (2007). Flat-Band Potential of a Semiconductor: Using the Mott–Schottky Equation. Journal of Chemical Education, 84(4): 685

Gopakumar A, Ren P, Chen J, Manzolli Rodrigues B V, Vincent Ching H Y, Jaworski A, Doorslaer S V, Rokicińska A, Kuśtrowski P, Barcaro G, Monti S, Slabon A, Das S (2022). Lignin-Supported Heterogeneous Photocatalyst for the Direct Generation of H_2O_2 from Seawater. Journal of the American Chemical Society, 144(6): 2603-2613

Hasnan N S N, Mohamed M A, Nordin N A, Wan Ishak W N R, Kassim M B (2023). Microtubular cellulose-derived kapok fibre as a solid electron donor for boosting photocatalytic H_2O_2 production over C-doped g-C_3N_4 hybrid complexation. Carbohydrate Polymers, 317: 121096

Hou S, Gao X, Lv X, Zhao Y, Yin X, Liu Y, Fang J, Yu X, Ma X, Ma T, Su D (2024). Decade Milestone Advancement of Defect-Engineered g-C_3N_4 for Solar Catalytic Applications. Nano-Micro Letters, 16(1): 70

Hou S, Yu C, Song X, Ding Y, Chang J, Liu Y, Chen L, Wei Q, Zhang X, Qiu J (2023). Modulating In-Plane Defective Density of Carbon Nanotubes by Graphitic Carbon Nitride Quantum Dots for Enhanced Triiodide Reduction. Advanced Functional Materials, 33(23): 2212112

Isaka Y, Kawase Y, Kuwahara Y, Mori K, Yamashita H (2019). Two-Phase System Utilizing Hydrophobic Metal–Organic Frameworks (MOFs) for Photocatalytic Synthesis of Hydrogen Peroxide. Angewandte

Chemie International Edition, 58(16): 5402-5406
Jiang Z, Li C, Qi F, Wang Z, Liu Y, Li F, Wang H, Bian Z, Zhu M, Kumirska J, Siedlecka E M (2025). A Review on Photocatalytic Hydrogen Peroxide Production from Oxygen: Material Design, Mechanisms, and Applications. ACS Applied Materials & Interfaces, 17(1): 42-66
Kumar A, Rana S, Dhiman P, Sharma P, Lai C W, Sharma G (2025). Recent progress in integration of photocatalysis and nanofiltration for advanced wastewater treatment. Frontiers of Environmental Science & Engineering, 19(11): 150
Li S, Dong G, Hailili R, Yang L, Li Y, Wang F, Zeng Y, Wang C (2016a). Effective photocatalytic H_2O_2 production under visible light irradiation at g-C_3N_4 modulated by carbon vacancies. Applied Catalysis B: Environmental, 190: 26-35
Li X, Zhang G, Li N, Xu Q, Li H, Lu J, Chen D (2024). Solar-driven production of highly concentrated hydrogen peroxide by $Zn_3In_2S_6$/PCN-222 heterostructure. Nano Energy, 126: 109671
Li Y, Ho W, Lv K, Zhu B, Lee S C (2018). Carbon vacancy-induced enhancement of the visible light-driven photocatalytic oxidation of NO over g-C_3N_4 nanosheets. Applied Surface Science, 430: 380-389
Li Y, Ouyang S, Xu H, Wang X, Bi Y, Zhang Y, Ye J (2016b). Constructing Solid–Gas-Interfacial Fenton Reaction over Alkalinized-C_3N_4 Photocatalyst To Achieve Apparent Quantum Yield of 49% at 420 nm. Journal of the American Chemical Society, 138(40): 13289-13297
Li Z, Mercado C C, Yang M, Palay E, Zhu K (2017). Electrochemical impedance analysis of perovskite–electrolyte interfaces. Chemical Communications, 53(16): 2467-2470
Li Z, Zhou Y, Zhou Y, Wang K, Yun Y, Chen S, Jiao W, Chen L, Zou B, Zhu M (2023). Dipole field in nitrogen-enriched carbon nitride with external forces to boost the artificial photosynthesis of hydrogen peroxide. Nature Communications, 14(1): 5742
Liao Z, He H, Liu F, Cui J, Guo Z, Abdulaziz A-A, Huang B, Sun H, Pan X (2026). Synergy mechanisms of algal extracellular organic matter and manganese oxides in 17α-ethinylestradiol photochemical degradation. ENGINEERING Environment, 20(4): 56
Liao Z, Hou H, Du J, Wang L, Wang S, Wang S, Zhan X, Yang H, Yang D, Yang W (2025). Engineering vacancy-defective carbon nitride nanowire clusters for dramatically enhanced visible-light-driven photocatalytic H2O2 production. Journal of Materials Chemistry A, 13(14): 9849-9864
Liu C, Bao T, Yuan L, Zhang C, Wang J, Wan J, Yu C (2022). Semiconducting MOF@ZnS Heterostructures for Photocatalytic Hydrogen Peroxide Production: Heterojunction Coverage Matters. Advanced Functional Materials, 32(15): 2111404
Liu P, Liang T, Li Y, Zhang Z, Li Z, Bian J, Jing L (2024). Photocatalytic H_2O_2 production over boron-doped g-C_3N_4 containing coordinatively unsaturated FeOOH sites and CoOx clusters. Nature Communications, 15(1): 9224
Liu Q, Bi H, Zhao R, Yang X, Chen F, Shen Z (2025). Fully Exposed Silver Clusters Enabling Highly Efficient Photocatalytic H_2O_2 Production in Pure Water. Angew Chem Int Ed Engl, 64(37): e202511687
Liu Z-L, Zhou J-L, Yuan S-X, Zhang M-R, Zhang M, Lu T-B Asymmetry-Engineered g-2C_3N_4 Nanosheets with Dual Electronic-Adsorption Modulation for High-Efficiency Solar-Driven H_2O_2 Synthesis. Advanced Functional Materials, 36(20): e23126
Lu Y, Guo Y, Zhang S, Li L, Jiang R, Zhang D, Yu J C, Wang J (2024). Promoting Proton Donation through Hydrogen Bond Breaking on Carbon Nitride for Enhanced H_2O_2 Photosynthesis. ACS Nano, 18(31): 20435-20448
Luo J, Wei X, Qiao Y, Wu C, Li L, Chen L, Shi J (2023). Photoredox-Promoted Co-Production of Dihydroisoquinoline and H_2O_2 over Defective $Zn_3In_2S_6$. Advanced Materials, 35(10): 2210110

Patra P, Mohapatra Y (2021). Dielectric constant of thin film graphitic carbon nitride (g-C 3 N 4) and double dielectric Al 2 O 3 /g-C 3 N 4. Applied Physics Letters, 118: 103501

Ricciardulli T, Gorthy S, Adams J S, Thompson C, Karim A M, Neurock M, Flaherty D W (2021). Effect of Pd Coordination and Isolation on the Catalytic Reduction of O_2 to H_2O_2 over PdAu Bimetallic Nanoparticles. Journal of the American Chemical Society, 143(14): 5445-5464

Sánchez M, Torres E, Ramos D R, Aguilar S D, Fernández M I, Ruiz I, Canle M, Soto M (2025). Elimination of faecal indicator microorganisms from wastewater by combining constructed wetlands and heterogeneous photocatalysis: from laboratory to pilot-scale implementation. Frontiers of Environmental Science & Engineering, 19(12): 174

Sha Z, Hu C, Tu S, Li T, Chen F, Huang H (2025). Piezo-activating oxygen vacancy regulates quantum well effect and p-band center for exceptional photocatalysis. Nano Energy, 139: 110919

Shan T, Li J, Wu S, Wu H, Zhang F, Liao G, Xiao H, Huang L, Chen L (2023). Boosting H2O2 production over carboxymethyl cellulose modified g-C_3N_4 via hydrogen-bonding-assisted charge transfer. Chemical Engineering Journal, 478: 147509

Shan T, Wang Y, Luo D, Huang Z, Zhang F, Wu H, Huang L, Li J, Chen L, Xiao H (2024). Extended H-bonds/π-bonds networks for boosting electron transfer over polydopamine-covered nanocellulose/g-C3N4 toward efficient photocatalytic H2O2 production. Applied Catalysis B: Environment and Energy, 349: 123872

Shen M, Zhang L, Wang M, Tian J, Jin X, Guo L, Wang L, Shi J (2019). Carbon-vacancy modified graphitic carbon nitride: enhanced CO_2 photocatalytic reduction performance and mechanism probing. Journal of Materials Chemistry A, 7(4): 1556-1563

Shi J, Wang H, Nie J, Yang T, Ju C, Pu K, Shi J, Zhao T, Li H, Xue J (2023). Alkali-assisted engineering of ultrathin graphite phase carbon nitride nanosheets with carbon vacancy and cyano group for significantly promoting photocatalytic hydrogen peroxide generation under visible light: Fast electron transfer channel. Journal of Colloid and Interface Science, 643: 47-61

Shi L, Yang L, Zhou W, Liu Y, Yin L, Hai X, Song H, Ye J (2018). Photoassisted Construction of Holey Defective g-C_3N_4 Photocatalysts for Efficient Visible-Light-Driven H_2O_2 Production. Small, 14(9): 1703142

Shiraishi Y, Kanazawa S, Sugano Y, Tsukamoto D, Sakamoto H, Ichikawa S, Hirai T (2014). Highly Selective Production of Hydrogen Peroxide on Graphitic Carbon Nitride (g-C3N4) Photocatalyst Activated by Visible Light. ACS Catalysis, 4(3): 774-780

Sun Y, Han L, Strasser P (2020). A comparative perspective of electrochemical and photochemical approaches for catalytic H_2O_2 production. Chemical Society Reviews, 49(18): 6605-6631

Tan L, Chen Y, Li D, Wang S, Ao Z (2022). WSe_2/g-C_3N_4 for an In Situ Photocatalytic Fenton-like System in Phenol Degradation. Nanomaterials (Basel), 12(18): 3089

Tian J, Feng B, Zhang X, Gu K, Pei Y, Qiao M, Zhang J, Zong B (2023). One-step nitrogen defect engineering of polymeric carbon nitride for visible light-driven photocatalytic O_2 reduction to H_2O_2. Journal of Colloid and Interface Science, 634: 138-147

Wang L, Zhang J, Zhang Y, Yu H, Qu Y, Yu J (2022). Inorganic Metal-Oxide Photocatalyst for H_2O_2 Production. Small, 18(8): 2104561

Wen D, Su Y, Fang J, Zheng D, Xu Y, Zhou S, Meng A, Han P, Wong C-P (2023). Synergistically boosted photocatalytic production of hydrogen peroxide via protonation and oxygen doping on graphitic carbon nitride. Nano Energy, 117: 108917

Xie Y, Li Y, Huang Z, Zhang J, Jia X, Wang X-S, Ye J (2020). Two types of cooperative nitrogen

vacancies in polymeric carbon nitride for efficient solar-driven H2O2 evolution. Applied Catalysis B: Environmental, 265: 118581

Xu S, Yu Y, Zhang X, Xue D, Wei Y, Xia H, Zhang F, Zhang J-N (2024). Enhanced Electron Delocalization Induced by Ferromagnetic Sulfur doped C_3N_4 Triggers Selective H_2O_2 Production. Angewandte Chemie International Edition, 63(39): e202407578

Xue Y, Ji Y, Wang X, Wang H, Chen X, Zhang X, Tian J (2023). Heterostructuring noble-metal-free 1T' phase MoS_2 with g-C_3N_4 hollow nanocages to improve the photocatalytic H_2 evolution activity. Green Energy & Environment, 8(3): 864-873

Yan S C, Li Z S, Zou Z G (2009). Photodegradation performance of g-C_3N_4 fabricated by directly heating melamine. Langmuir, 25(17): 10397-10401

Yang P, Wang L, Zhuzhang H, Wang R, Titirici M-M, Wang X (2019a). Photocarving nitrogen vacancies in a polymeric carbon nitride for metal-free oxygen synthesis. Applied Catalysis B: Environmental, 256: 117794

Yang S, Si D, Zou L, Shi M, Huang Y, Cao R (2025). Engineering Imine Carbon Catalytic Sites in Covalent Organic Frameworks for Enhanced Overall H_2O_2 Photosynthesis. Journal of the American Chemical Society, 147(33): 30287-30295

Yang Y, Zeng Z, Zeng G, Huang D, Xiao R, Zhang C, Zhou C, Xiong W, Wang W, Cheng M, Xue W, Guo H, Tang X, He D (2019b). Ti_3C_2 Mxene/porous g-C_3N_4 interfacial Schottky junction for boosting spatial charge separation in photocatalytic H_2O_2 production. Applied Catalysis B: Environmental, 258: 117956

Yao C, Shan J, Liu J, Luo J, Pan L, Lyu J, Feng F, Lin L, Lu C, Zheng Y, Wang J, Wang Q, Zhang Q, Li X (2024). Gating effect of g-C_3N_4-encapsulated Pt-based catalysts for the hydrogenation and Bamberger rearrangement of nitroaromatics. Journal of Materials Chemistry A, 12(48): 33606-33616

Yu W, Hu C, Bai L, Tian N, Zhang Y, Huang H (2022). Photocatalytic hydrogen peroxide evolution: What is the most effective strategy? Nano Energy, 104: 107906

Yu X, Wei Z, Qin Y, Zhang X, Hao D, Jing L, Liu Y, Dai H, Deng J, Zhu Y (2025). Functional Groups-Regulated Organic Semiconductors for Efficient Artificial Photosynthesis of Hydrogen Peroxide. Advanced Materials, 37(17): 2501494

Zhai H, Tan P, Lu L, Liu H, Liu Y, Pan J (2021). Abundant hydroxyl groups decorated on nitrogen vacancy-embedded g-C_3N_4 with efficient photocatalytic hydrogen evolution performance. Catalysis Science & Technology, 11(11): 3914-3924

Zhang E, Zhu Q, Huang J, Liu J, Tan G, Sun C, Li T, Liu S, Li Y, Wang H, Wan X, Wen Z, Fan F, Zhang J, Ariga K (2021a). Visually resolving the direct Z-scheme heterojunction in CdS@$ZnIn_2S_4$ hollow cubes for photocatalytic evolution of H_2 and H_2O_2 from pure water. Applied Catalysis B: Environmental, 293: 120213

Zhang F, Lv X, Wang H, Cai J, Wang H, Bi S, Wei R, Yang C, Zheng G, Han Q (2025a). p-π Conjugated Covalent Organic Frameworks Expedite Molecular Triplet Excitons for H_2O_2 Production Coupled with Biomass Upgrading. Advanced Materials, 37(17): 2502220

Zhang R, Zhang X, Liu S, Tong J, Kong F, Sun N, Han X, Zhang Y (2021b). Enhanced photocatalytic activity and optical response mechanism of porous graphitic carbon nitride (g-C_3N_4) nanosheets. Materials Research Bulletin, 140: 111263

Zhang X, Xin H, Hou C, Zhang G, Ji Q, Liu H (2025b). Enhancing the performance of hydrogen peroxide electrosynthesis via anode-cathode coupling and pulsed electrolysis. Frontiers of Environmental Science & Engineering, 19(11): 145

Zhang Y, Wu D, Zeng X, Qiu B, Zhu Q, Zhang J (2025c). H_2O_2 Production via Artificial Photosynthesis Over Defective Graphitic Carbon Nitride. Advanced Science, 12(33): e07913
Zhao L, Wang Y, Wen G, Zhang X, Huang X (2025). Layered g-C_3N_4/MoS_2 Nanocomposites as Anode Materials for Lithium Ion Storage. ACS Applied Nano Materials, 8(19): 9937-9948
Zhao S, Zhao X (2018). Polyoxometalates-derived metal oxides incorporated into graphitic carbon nitride framework for photocatalytic hydrogen peroxide production under visible light. Journal of Catalysis, 366: 98-106
Zhao S, Zhao X (2019). Insights into the role of singlet oxygen in the photocatalytic hydrogen peroxide production over polyoxometalates-derived metal oxides incorporated into graphitic carbon nitride framework. Applied Catalysis B: Environmental, 250: 408-418
Zhao S, Zhao X, Zhang H, Li J, Zhu Y (2017). Covalent combination of polyoxometalate and graphitic carbon nitride for light-driven hydrogen peroxide production. Nano Energy, 35: 405-414
Zheng D, Wu Y, Yang X, Wang S, Fang Y (2024). Developing Polymeric Carbon Nitrides for Photocatalytic H_2O_2 Production. ChemSusChem, 17(20): e202400528
Zhou J, Shan T, Luo H, Boury B, Xu X, Wu H, Zhang F, Xiao H (2023). Enhanced single-electron transfer for efficiently photocatalytic H_2O_2 production over g-C_3N_4 decorated with TEMPO-oxidized cellulosic carbon. Journal of Environmental Chemical Engineering, 11(2): 109512
Zhou Y-Y, Yuan C-J, Wu Z-J, Zhang J, Xu B-J, Cao J-Y, Lee M-Y, Chen Z, Du Y (2025). Bromide and its associated brominated disinfection byproducts: occurrence, toxicity and control strategies. Frontiers of Environmental Science & Engineering, 19(1): 8
Zhu Y, Zhang H, Liu H, He G, Liu X, Xiao J, Sun Y, Han L (2022). Water-activated formation of porous graphitic carbon nitride with carbon vacancies to boost photocatalytic hydrogen peroxide production. Chemical Communications, 58(72): 10084-10087